Journal of Power Sources 187 (2009) 431–443

Contents lists available at ScienceDirect

Journal of Power Sources

journal homepage: www.elsevier.com/locate/jpowsour

Two-phase flow and maldistribution in gas channels of a polymer electrolyte fuel cell

Suman Basu*, Jun Li, Chao-Yang Wang

Department of Mechanical and Nuclear Engineering, and Electrochemical Engine Center (ECEC), The Pennsylvania State University, University Park, PA 16802, United States

ARTICLE INFO

Article history:
Received 7 October 2008
Received in revised form 7 November 2008
Accepted 7 November 2008
Available online 21 November 2008

Keywords:
PEFC
Two-phase flow
Gas channel
Flow maldistribution
Pressure drop

ABSTRACT

Liquid water transport in a polymer electrolyte fuel cell (PEFC) is a major issue for automotive applications. Mist flow with tiny droplets suspended in gas has been commonly assumed for channel flow while two-phase flow has been modeled in other cell components. However, experimental studies have found that two-phase flow in the channels has a profound effect on PEFC performance, stability and durability. Therefore, a complete two-phase flow model is developed in this work for PEFC including two-phase flow in both anode and cathode channels. The model is validated against experimental data of the wetted area ratio and pressure drop in the cathode side. Due to the intrusion of soft gas diffusion layer (GDL) material in the channels, flow resistance is higher in some channels than in others. The resulting flow maldistribution among PEFC channels is of great concern because non-uniform distributions of fuel and oxidizer result in non-uniform reaction rates and thus adversely affect PEFC performance and durability. The two-phase flow maldistribution among the parallel channels in an operating PEFC is explored in detail.

1. Introduction

The portability, compactness, zero emission and high power output at low temperature has made the polymer electrolyte fuel cell (PEFC) one of the most potent replacements for the internal combustion engines [1]. This new focus has led to an urgent need for identification, understanding, prediction, control, and optimization of various transport and electrochemical processes that occur on disparate length scales in fuel cells [2]. Recent studies have shown that among all transport phenomena, the two-phase transport of water in the PEFC to maintain water balance is the most critical to cell performance.

A typical PEFC and its components are schematically displayed in Fig. 1a. A PEFC model should consider transport phenomena with electrochemical kinetics and charge transport of both electrons and protons in disparate length and time scales [2]. The need for detailed model validation has been increasingly acknowledged by the PEFC research community because the global current–voltage curve is largely inadequate to differentiate various transport and electrochemical processes.

Much effort has been directed toward PEFC modeling [2–5]. Although water is essential for membrane proton conductivity, excess water can initiate channel flooding, blocking the pores of GDL and catalyst layer and hampering the reactant transport [6,7]. Channel flooding refers to a situation where a substantial fraction of liquid water accumulates in gas channels. Given the low startup temperatures (room temperature) for automobile applications, two-phase flow is unavoidable for automobile fuel cells. Therefore, its understanding and prediction is critical for good PEFC design. Two-phase transport in a PEFC consists of three subprocesses: (1) liquid water accumulation and transport in catalyst layers, (2) two-phase transport in GDL and MPLs, along with the interfacial coverage at the GDL surface, and (3) two-phase flow in gas channels. All two-phase flow modeling efforts in PEFC in the literature were on the first two sub-processes [8–13]. Ample experimental evidence, however, indicates that the channel flooding plays a pivotal role in water management, particularly at low current densities where gas velocity is insufficiently low to drain liquid water out of the channels. The low load regime is particularly important for PEFC engines due to its potential of high energy conversion efficiency and it is most frequently used.

The flooding problem is compounded by GDL intrusion into the channels. PEFC is operated under high compression to minimize the contact resistance between the land and GDL. The high compression pressure pushes the softer GDL material into the channel, blocking the channels partially as shown in Fig. 1b. Compression pressure is highest at the edge (near the location of tightening bolts) and therefore GDL intrusion is most severe at the edge channels. Flow through the intruded channel is reduced under the same pressure drop, thereby making it more difficult to flush liquid water out of

* Corresponding author. Tel.: +1 814 865 9768.
E-mail address: sxb967@psu.edu (S. Basu).

0378-7753/$ – see front matter © 2008 Elsevier B.V. All rights reserved.
doi:10.1016/j.jpowsour.2008.11.039

Nomenclature

A	area
C_i	local concentration of species i, mol m^{-3}
D_i	diffusion coefficient of species i, m^2 s^{-1}
d	diameter
I	current density, A cm^{-2}
K	permeability of the porous media
k	relative permeability of the phase
M	molecular weight
mf_l^k	mass fraction of species k in liquid phase
n	normal direction
P	pressure, Pa
S	source term in the governing equations
s	liquid water saturation/volume fraction
T	absolute temperature, K
u	velocity
x	x coordinate, μm
y	y coordinate, μm
z	z coordinate, μm

Greek letters

α	net water transport coefficient
ρ	density
ε	porosity
γ	correction factor
κ	electrolyte conductivity, S m^{-1}
λ	relative mobility
σ	surface tension coefficient (N m^{-1})
ξ	Stoichiometry at gas channel inlet (anode or cathode)
ν	kinematic viscosity

Subscripts and superscripts

g	gas phase
l	liquid species
eff	effective
sat	saturation
r	relative
c	convective correction
mem	membrane
in	inlet
ph	phase
avg	average
H_2O	water
O_2	oxygen

the channel. This exacerbates channel flooding and accelerates the mass transport loss as well as leads to operational instability. The worst scenario is total blockage of a channel by liquid water. The maldistribution of flow in parallel channels has profound performance and durability implications, and a serious loss of efficiency is possible as the whole channel is lost due to blockage. Hence, for a PEFC to maintain stable performance, flooding of the channels must be avoided.

Channel flooding in PEFCs has received increased attention in the fuel cell community [14–26]. A friction factor similar to that in the case of laminar flow through a circular channel was proposed for the PEFC channels [14]. Preferential entry of inlet flow in parallel channels was attributed partly to the formation of recirculation vortex at the inlet [15]. Single-phase flow in the channel has been used widely in the gas channel for design purposes [16,17,18] but experimental observations indicate presence of liquid water in the PEFC gas channels [19,20]. Attempts have been made to use analytically calculated dry length of a gas channel as a design tool for PEFC channel flow field design [21]. Others used the void-in-fluid (VOF) method [22–26] to compute two-phase flow in the gas channels. Unfortunately, these models are computationally expensive and have not been integrated with the other components of a PEFC.

Few experimental investigations on flow distribution in the PEFC channels exist in literature [14,19,20,27]. While mist flow model and film flow model have been used for the extreme cases of high gas velocity (liquid volume fraction <0.1%) and low gas velocity/highly hydrophilic channel wall (liquid volume fraction >10%), respectively, a general model covering a common range of liquid fraction and capable of capturing flow maldistribution was absent. Such a general model will enable the prediction of channel flooding, two-phase flow maldistribution in multiple, parallel channels, and the flow-field effect on liquid water removal in operating PEFCs.

In the present work, we first couple a recently developed two-phase channel flow model with other two-phase models for the catalyst layer and GDL previously developed in our laboratory to form a complete two-phase model for an entire PEFC. The channel two-phase model [28,29] is based on the framework of multi-phase mixture model (M^2 model) and capable of predicting the liquid water volume fraction and pressure along the flow direction. Then, the complete model is validated against experimental data of wetted area ratio and pressure drop over a range of operating conditions. Finally, this complete two-phase model is employed to study the effects of GDL intrusion and manifold design on reducing flow maldistribution.

2. Mathematical model

A PEFC consists of seven sub-regions – anode gas channel, anode GDL, anode catalyst layer, ionomeric membrane, cathode catalyst layer, cathode GDL and cathode gas channel. In addition, the electron transport through bipolar plates may be important in some cases [30]. The membrane is a solid-state electrolyte with water and proton co-transport taking place through its ionomer phase. Full descriptions of electrochemical and transport phenomena in a PEFC already exist in the literature [2] and are not repeated here.

Two-phase flow and transport in a PEFC are governed by the laws of momentum, mass, energy, species and charge conservation. Under non-isothermal, two-phase conditions the conservation equations of mass, momentum, energy, species and charge equations in the PEFC can be written as [30–32]

$$\text{Mass}: \quad \nabla\cdot(\rho\vec{u}) = 0 \tag{1}$$

$$\text{Momentum}: \quad \frac{1}{\varepsilon^2}\nabla\cdot(\rho\vec{u}\vec{u}) = -\nabla P - \nabla\cdot(\rho\tau) + S_u \tag{2}$$

$$\text{Energy}: \quad \nabla\cdot(\gamma_T\rho C_p\vec{u}T) = \nabla\cdot(k_{eff}\nabla T) + S_T \tag{3}$$

$$\text{Species}: \quad \nabla\cdot(\gamma_c\vec{u}C^k) = \nabla\cdot(D_g^{k,eff}\nabla C_g^k) - \nabla\cdot\left[\left(\frac{mf_l^k}{M^k} - \frac{C_g^k}{\rho_g}\right)\vec{j}_l\right] + S_k \tag{4}$$

$$\text{Charge (electrons)}: \quad \nabla\cdot(\sigma^{eff}\nabla\Phi_s) + S_{\Phi_s} = 0 \tag{5}$$

$$\text{Charge (protons)}: \quad \nabla\cdot(k^{eff}\nabla\Phi_e) + S_{\Phi_e} = 0 \tag{6}$$

The source terms are tabulated in Table 1. Details about these equations and the source terms are available in the literature [31,32]. The present modeling approach is to view all components in a PEFC as porous media. Specially, we model flow channels of typical dimension between 0.2 and 1 mm as a structured porous media or a bundle of straight capillary tubes. Hence, we apply the two-phase flow theory based on extended Darcy's law to describe two-phase

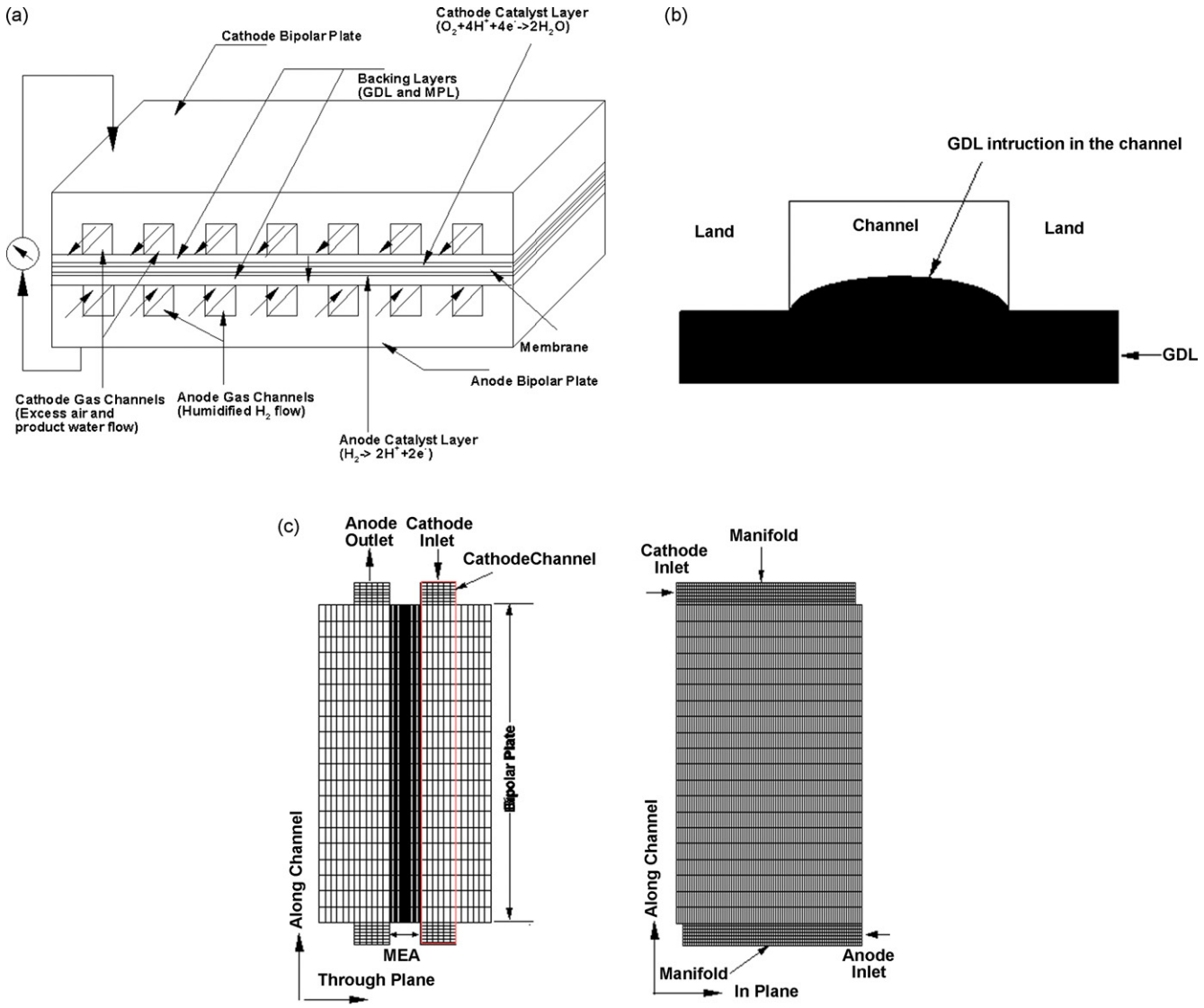

Fig. 1. (a) Schematic of a multi-channel counter-flow PEFC. (b) Schematic of a typical GDL intrusion in a channel. (c) Sections of the computational mesh.

flow and transport throughout an entire PEFC including the flow channels. Furthermore, for convenience of numerical implementation, the two-phase theory in porous media is formulated into M^2 model without making any additional assumptions [8,11,12,32,33]. The validity of this porous medium approach for channel two-phase flow encountered in PEFCs has been explored in detail elsewhere [28,29].

Assuming a local thermodynamic equilibrium between the liquid and vapor phases in the two-phase region, the water concentration in the vapor phase could be taken as equal to the saturation water concentration that solely depends on the temperature. Since the liquid phase consists of only water, the water mole fraction in the liquid is equal to unity. Therefore, the total water concentration C^{H_2O} to be solved by Eq. (4) can be written as

$$C^{H_2O} = sC_l^{H_2O} + (1-s)C_g^{H_2O} = s\left(\frac{\rho_l}{M_{H_2O}}\right) + (1-s)C_{sat}^{H_2O} \quad (7)$$

Table 1
Source terms for the conservation equations in each sub-region.

	S_u	$S_C^{H_2O}$	S_C (for reactants)	S_{ϕ_s}	S_{Φ_e}
Channels	$-\frac{\mu}{K_{GDL}}\vec{u}$	0	0	0	–
Gas diffusion layers	$-\frac{\mu}{K_{GDL}}\vec{u}$	$-\dot{q}_{gs}^{H_2O}$	0	0	–
Catalyst layers	$-\frac{\mu}{K_{CL}}\vec{u}$	$-\nabla\cdot\left(\frac{n_d}{F}\vec{i}_e\right) - \frac{s_k j}{nF}$	$-\left(\frac{s_k j}{nF}\right)$	$-j$	j
Membrane	–	$-\nabla\cdot\left(\frac{n_d}{F}\vec{i}_e\right)$	0	–	0

Note: Electrochemical reaction where $\sum s_k M_k^z = ne^-$ $\begin{pmatrix} M_k \equiv \text{chemical formula of species } k \\ s_k \equiv \text{stoichiometry coefficient} \\ n \equiv \text{number of electrons transferred} \end{pmatrix}$. In PEFC, there are (anode) H_2–$2H^+ = 2e^-$; (cathode) $2H_2O$–O_2–$4H^+ = 4e^-$.

Table 2
Cell geometry and properties.

Description	Value
Cell length	100.0 mm
Gas channel depth	0.5 mm
Gas channel width	1.0 mm
Land width	1.0 mm
Anode/cathode GDL thickness	0.20 mm
Anode/cathode catalyst layers thickness	0.010 mm
Porosity of anode/cathode GDL, ε_{GDL}	0.6
Porosity of anode/cathode catalyst layers, ε_{CL}	0.6
Volume fraction of ionomer in anode/cathode catalyst layers, ε_e	0.18
Hydraulic permeability of anode/cathode GDL, K_{GDL}	3.0×10^{-14} m^2
Hydraulic permeability of membrane, K_{mem}	5.0×10^{-20} m^2
Contact angle of anode/cathode channel, GDL and catalyst layers, θ	60°, 110°, 110°
Contact resistance between catalyst layer and GDL, R_{GDL}	$1.0 \times 10^{-6}\ \Omega$ m^2
Anode/cathode inlet pressure, P_{in}	2.0 atm
Cell temperature, T_{cell}	80 °C

where s is the liquid water saturation or volume fraction. However, this summation does not indicate a mixing in molecular level. For any two-phase flow in any control volume we can calculate total water concentration as in Eq. (7) but it may not be possible to solve a conservation equation for it. Since pressure gradient and flow velocity are linearly coupled in porous media, it is possible to solve for the total water concentration instead of individual phases in porous media. From Eq. (7), the liquid saturation or volume fraction can be calculated from [31]

$$s = \frac{C^{H_2O} - C_{sat}^{H_2O}}{\rho_l/M_{H_2O} - C_{sat}^{H_2O}} \tag{8}$$

Within the M^2 model framework, the kinematic viscosity of the two-phase mixture is defined as

$$\nu = \left(\frac{k_{rl}}{\nu_l} + \frac{k_{rg}}{\nu_g}\right)^{-1} \tag{9}$$

where ν_l and ν_g are the kinematic viscosities of liquid and gas phases, respectively, while k_{rl} and k_{rg} are the relative permeabilities of liquid and vapor phases, respectively.

Table 3
Simulation parameters.

Description	Value
Exchange current density × ratio of reaction surface to catalyst layer volume in anode side, $ai_{0,a}^{ref}$	1.0×10^9 A m^{-3}
Exchange current density × ratio of reaction surface to catalyst layer volume in cathode side, $ai_{0,c}^{ref}$	2.0×10^4 A m^{-3}
Activation energy for oxygen reduction reaction in cathode side, E_a	73,269 J mol^{-1}
Reference hydrogen molar concentration, $c_{H_2,ref}$	40.88 mol m^{-3}
Reference oxygen molar concentration, $c_{O_2,ref}$	40.88 mol m^{-3}
Anodic and cathodic transfer coefficients for hydrogen oxidation reaction (HOR)	$\alpha_a = \alpha_c = 1$
Cathodic transfer coefficient for oxygen reduction reaction (ORR)	$\alpha_c = 1$
Dry membrane density, ρ^{mem}	2,000 kg m^{-3}
Equivalent weight of electrolyte in membrane, EW	1.1 kg mol^{-1}
Faraday constant, F	96,487 C mol^{-1}
Universal gas constant, R_u	8.314 J (mol K)$^{-1}$
Surface tension, σ	0.0625 N m^{-1}
Liquid water density, ρ_l (80 °C)	972 kg m^{-3}
Liquid water viscosity, μ_l	3.5×10^{-4} N s m^{-2}
Effective electronic conductivity in catalyst layers, σ_{CL}	1,000 S m^{-1}
Effective electronic conductivity in GDL, σ_{GDL}	10,000 S m^{-1}
Electronic conductivity in current collector, σ_{land}	20,000 S m^{-1}
Catalyst coverage coefficient, n_c	2.0
Diffusivity correction factor, n	2.3

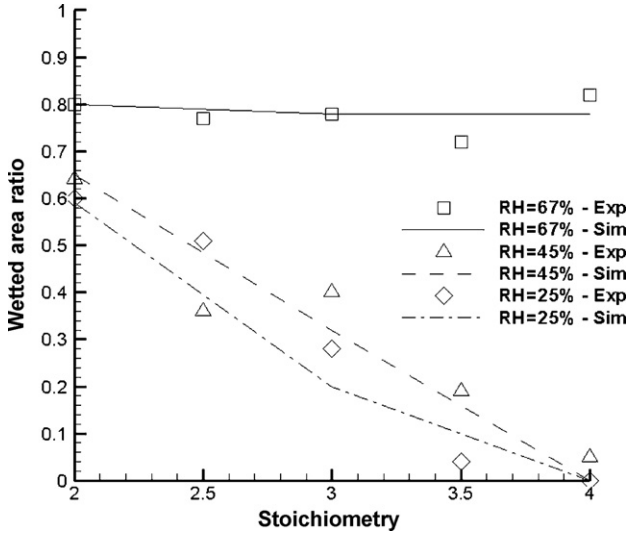

Fig. 2. Wetted area ratio versus air stoichiometry for $I_{avg} = 0.2$ A cm^{-2}.

Water is the only species that could be present in both liquid and vapor states. Therefore, the correction factor takes into account contributions due to both phases for water conservation equation. Other species can be present in only the gas phase. The species correction factor (γ_c) can be derived as follows [11]:

$$\gamma_c = \begin{cases} \dfrac{\rho}{C^{H_2O}}\left(\dfrac{\lambda_l}{M^{H_2O}} + \dfrac{\lambda_g}{\rho_g}C_{sat}\right) \\ \dfrac{\rho\lambda_g}{\rho_g(1-s)} \end{cases} \tag{10}$$

The mobility of each phase $\lambda_l(s)$ and $\lambda_g(s)$ are defined in Eqs. (11) and (12) in terms of the relative permeabilities of the liquid and gas and phases:

$$\lambda_l(s) = \frac{k_{rl}(s)/\nu_l}{k_{rl}(s)/\nu_l + k_{rg}(s)/\nu_g} \tag{11}$$

$$\lambda_g(s) = 1 - \lambda_l(s) \tag{12}$$

Two most important parameters to describe two-phase flows through a porous medium are relative permeability and capillary pressure functions. The relative permeabilities used in this work

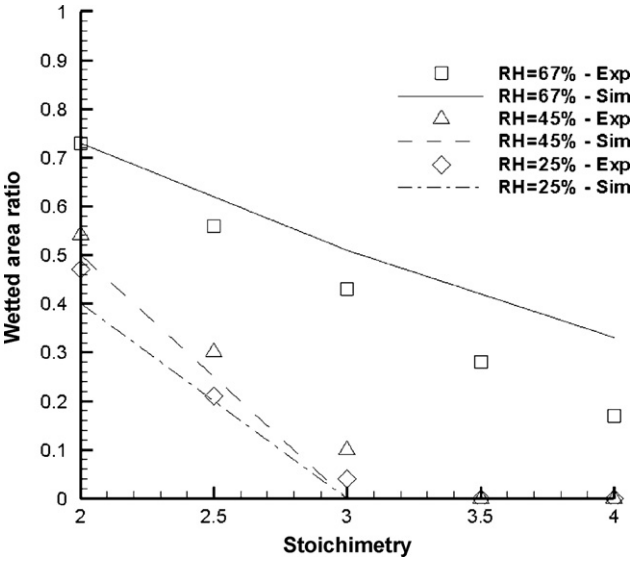

Fig. 3. Wetted area ratio versus air stoichiometry for $I_{avg} = 0.5$ A cm^{-2}.

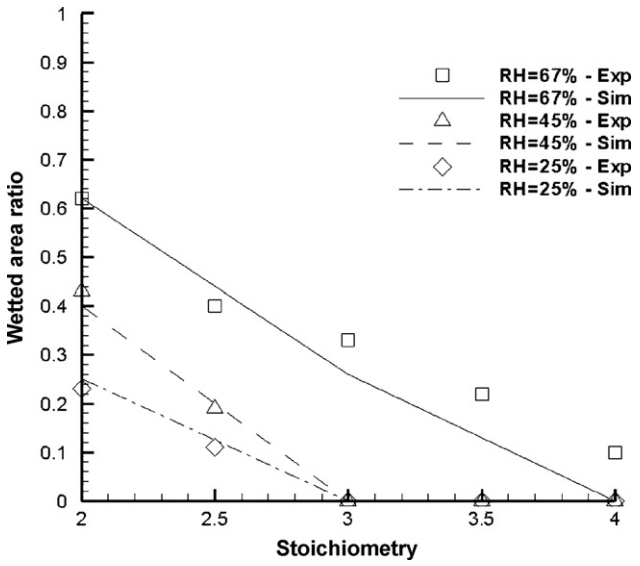

Fig. 4. Wetted area ratio versus air stoichiometry for $I_{avg} = 0.8\,A\,cm^{-2}$.

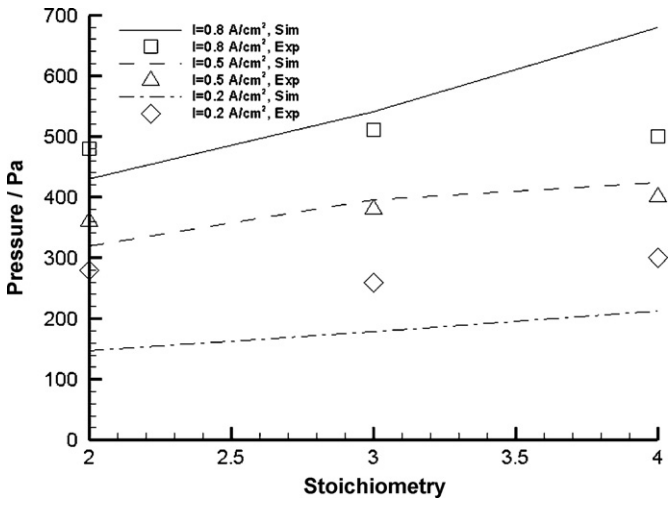

Fig. 5. Pressure drop validation with 33% GDL intrusion.

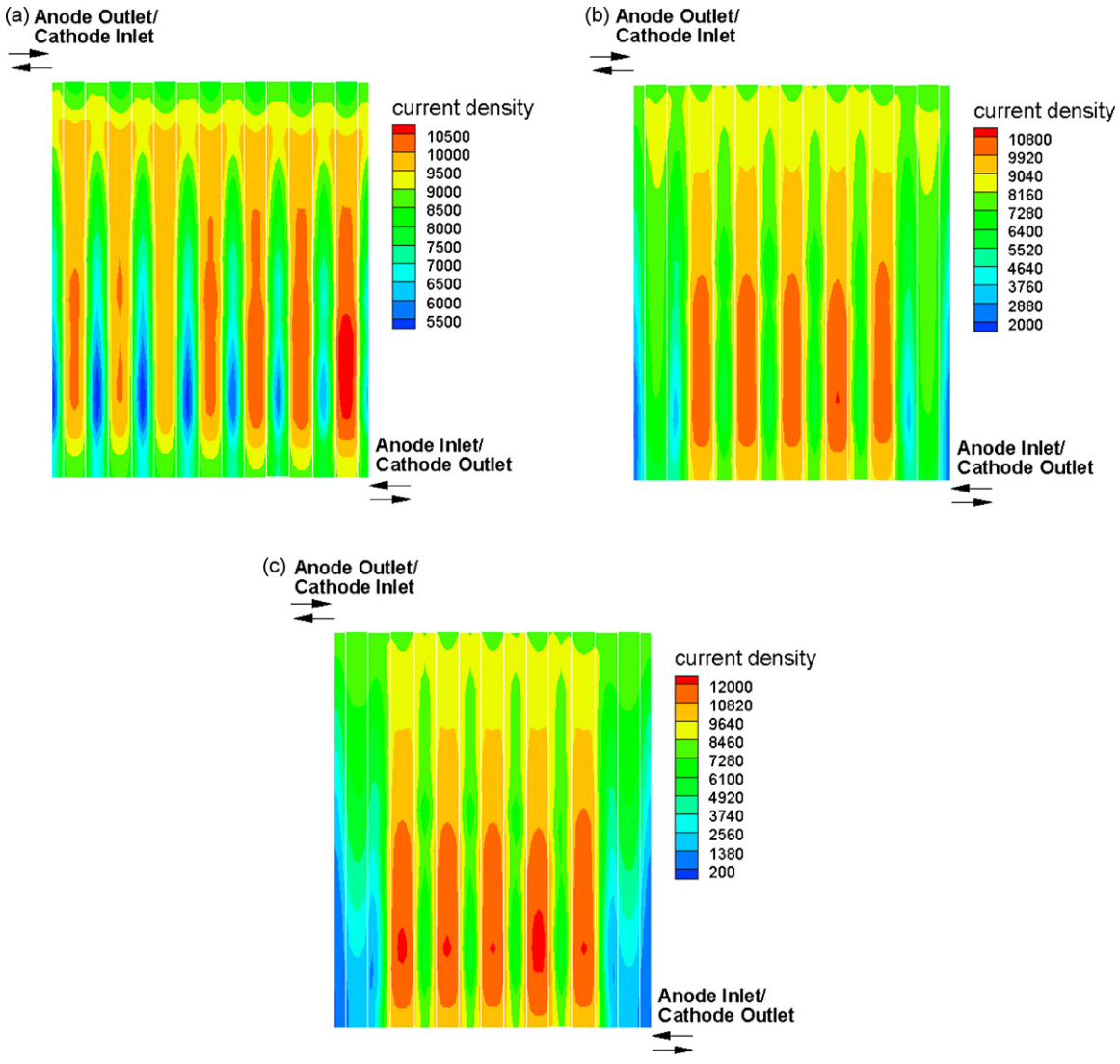

Fig. 6. Current density ($A\,m^{-2}$) contours in the membrane.

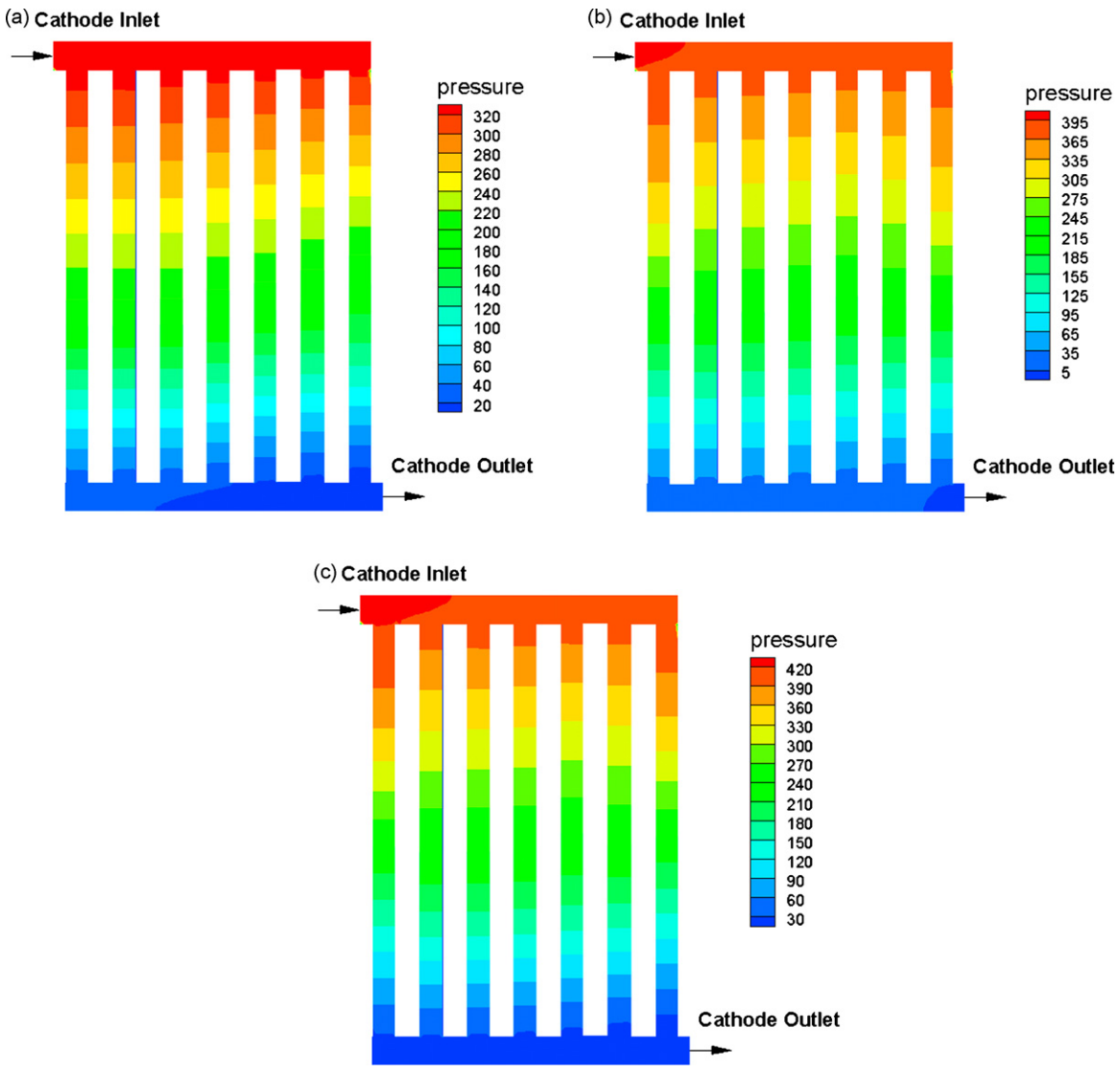

Fig. 7. Pressure (Pa) contours at the mid-height of cathode channels.

can be expressed as

$$k_{rl} = s^{n_k} \tag{13}$$

$$k_{rg} = (1-s)^{n_k} \tag{14}$$

where exponent n_k varies depending on the flow conditions and porous medium microstructures. Different values have been used for n_k [11,31,34] depending on flow situations. More recently it was found [28] that in the PEFC flow channels the value of n_k equal to 5 results in the best match with experimental pressure drop data. However, for different channel geometry and dimension fresh calibration with experimental data may be required. Therefore, in the present case, we use n_k equal to 5.0 in the channel and 4.0 otherwise.

Capillary pressure is usually expressed as Leverett function of the liquid saturation such that:

$$P_c = \sigma \cos(\theta_c)\left(\frac{\varepsilon}{K}\right)^{1/2} J(s) \tag{15}$$

We use the Leverett $J(s)$ function given by [5]

$$J(s) = \begin{cases} 1.417(1-s) - 2.120(1-s)^2 + 1.263(1-s)^3 & \text{for } \theta_c > 90^\circ \\ 1.417s - 2.120s^2 + 1.263s^3 & \text{for } \theta_c < 90^\circ \end{cases} \tag{16}$$

The absolute permeability K for the flow channels can be computed by numerical experiments of simulating single-phase flow through the flow channels. In the case of GDL intrusion, the channel cross-sectional area decreases. This would result in reduction in the absolute permeability. Consider that the absolute permeability through a minichannel can be expressed by [28]

$$K = c\frac{d_h^2}{32} \tag{17}$$

where c is the shape factor describing various cross-section geometries of the channels and d_h is the hydraulic diameter of the channel. Thus, one can use the following approximate expression for the absolute permeability in the intruded channels:

$$K_{intruded} = K_{unintruded}(1-\delta)^2 \tag{18}$$

where δ is the fraction reduction in the channel height due to GDL intrusion. The value of c could be calculated analytically for only a few regular cross-sections, for all other cross-sections it is calculated by matching the experimentally obtained pressure drop. Therefore, the effect of GDL roughness on pressure drop along channel could also be incorporated in this model.

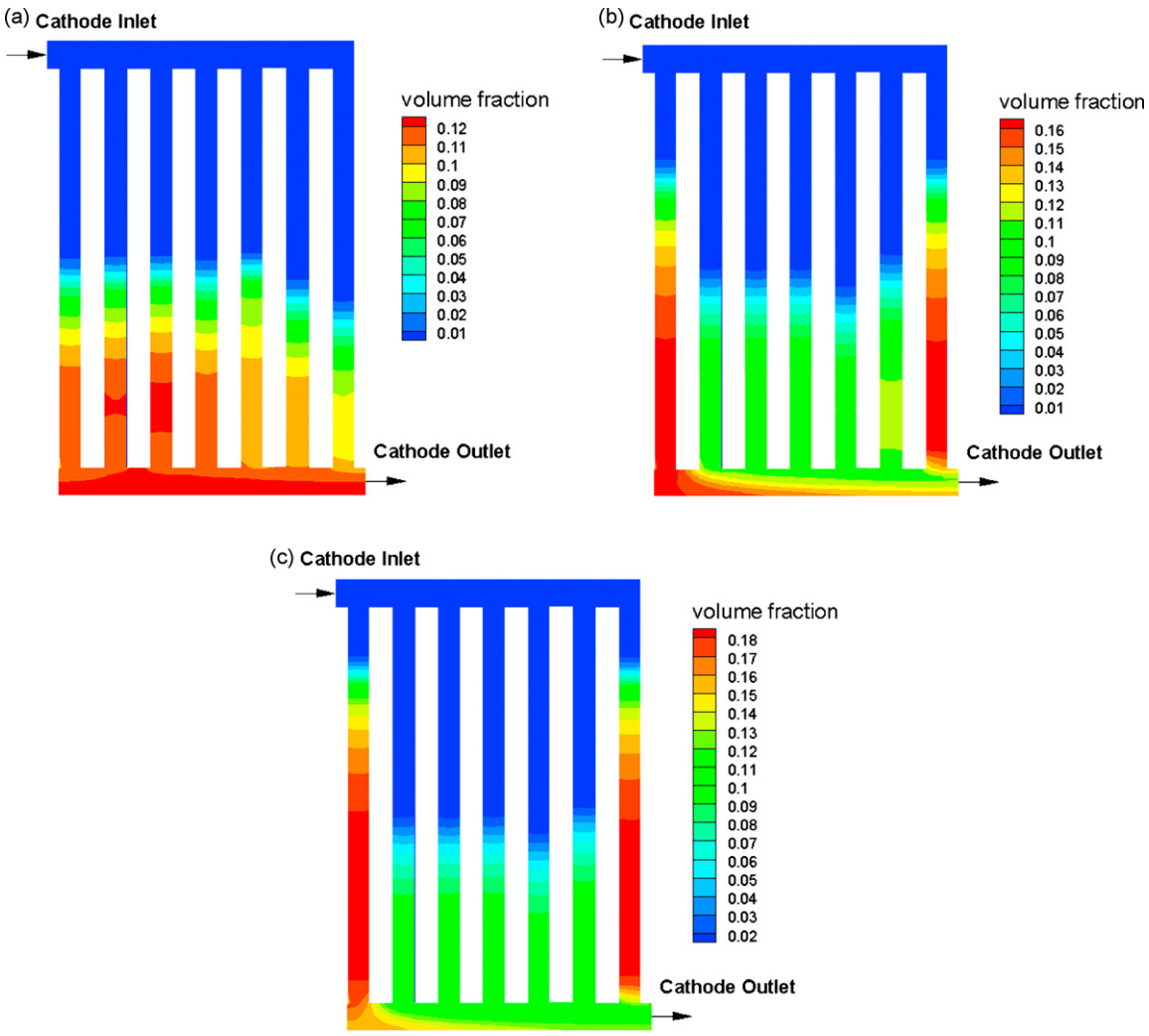

Fig. 8. Liquid water volume fraction contours at the mid-height of cathode channels.

3. Boundary conditions

The inlet velocity (u_{in}) is calculated in terms of cathode stoichiometry (ξ_c), average current density (I_{avg}), active area of the membrane (A_{mem}), molar concentration of oxygen (C^{O_2}) and the cross-sectional area of channels (A_{in}) as the following:

$$u_{in} = \frac{\xi_c I_{avg} A_{mem}}{4FC^{O_2}A_{in}} \tag{19}$$

where F is the Faraday constant.

The molar concentrations of species at the inlet are determined by the inlet pressure and humidity according to the ideal gas law.

The exit boundary is assumed to be fully developed namely:

$$\frac{\partial \vec{u}}{\partial n} = 0, \quad p = p_{ref}, \quad \frac{\partial C^k}{\partial n} = 0 \tag{20}$$

In this work the reference pressure is 2 atm.

At all wall boundaries we have:

$$\vec{u}.\hat{n} = 0, \quad \frac{\partial p}{\partial n} = 0, \quad \frac{\partial C^k}{\partial n} = 0. \tag{21}$$

4. Numerical procedures

The governing equations, Eqs. (3)–(8), along with their appropriate boundary conditions are discretized by the finite volume method and solved in a commercial flow solver, Fluent (version 6.1.22), by SIMPLE algorithm. The source terms and physical properties are implemented using the user-defined functions (UDF) available with commercial CFD software Fluent 6.1. Overall species balance and charge balance are checked in addition to the equation residuals as important convergence criteria. The cell geometry and the simulation parameters are listed in Tables 2 and 3. In the simulations to be presented below, all species imbalances are less than 1% and residuals smaller than 10^{-5}. Extensive grid independence test have been performed by Meng and Wang [35].

5. Results and discussion

5.1. Experimental validation

The most important predictive capabilities of our model include the fraction of the wet GDL–channel interface and the total two-phase pressure drop through the flow channels. Prediction of these quantities is therefore validated against the recent experiments of Hussaini and Wang [27]. A seven parallel channel 14 cm^2 active area cell, shown schematically in Fig. 1, is used in these experiments. The channels are 1 mm × 0.5 mm in cross-section and 100 mm in length. The membrane active area is 14 mm in width and 100 mm in length and the membrane is 30 μm thick Gore composite membrane. The computational mesh for this cell consists of 0.15 million grid points. Sections of this computational mesh are shown in Fig. 1c.

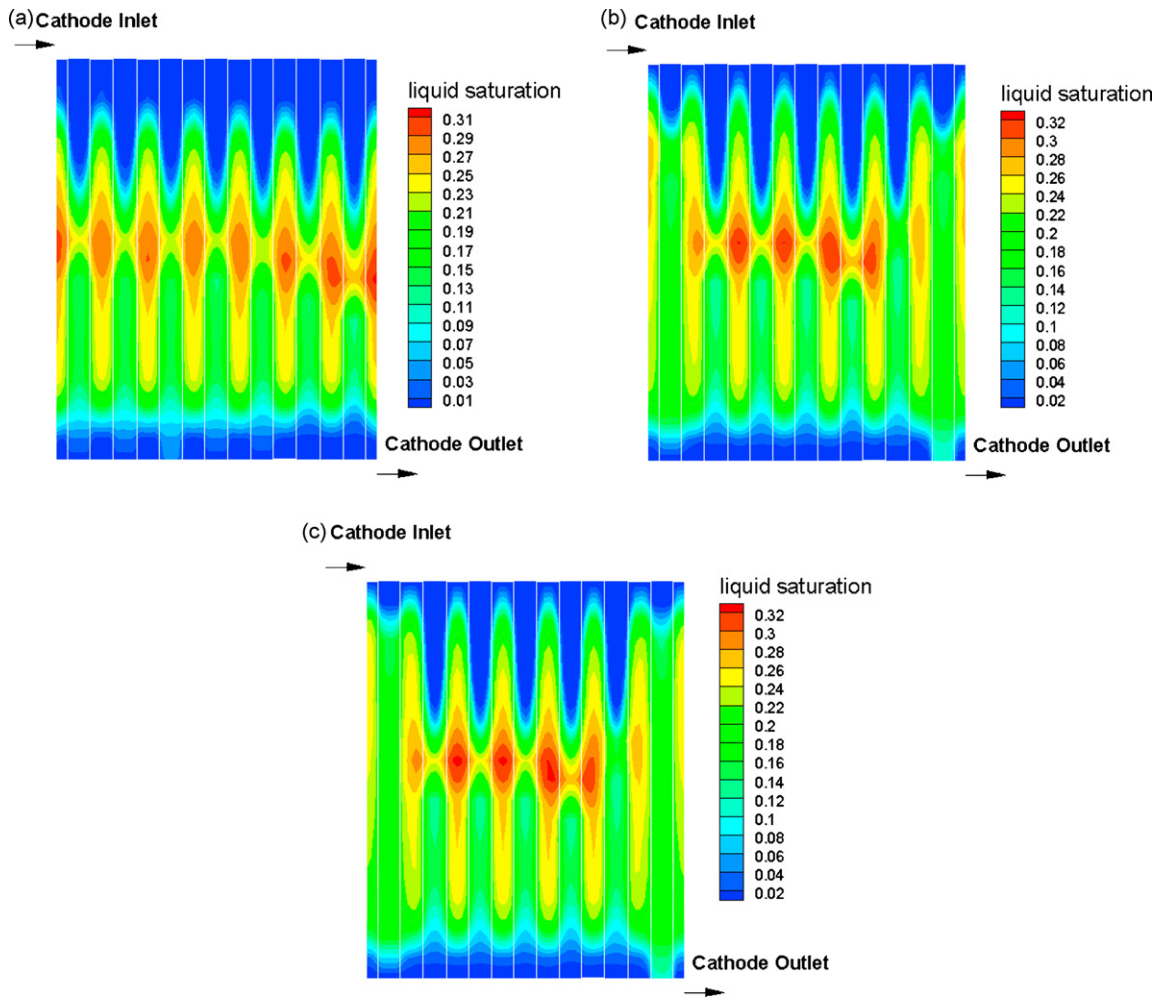

Fig. 9. Liquid water saturation contours at the midsection of the cathode GDL.

The wet area on the GDL–channel interface (covered partially by liquid water) is quantified from the flow visualization experiment on the seven-channel PEFC. The ratio of the wet area to the total GDL–channel interface area is defined as the "wetted area ratio". Here liquid saturation of 0.01 or greater is taken as wet area. An average of the wetted area ratio over the entire cell including all the channels is taken as the wetted area ratio for the PEFC at that operating condition. The wetted area ratio is a strong function of three operational parameters – the average current density, the air stoichiometry and the relative humidity at the cathode inlet. At low inlet relative humidity, ability of the cathode flow to carry water in vapor form is high. Therefore, low wetted area ratio is expected at low relative humidity. Similarly, at high air stoichiometry flow can carry more water in vapor form and as a result wetted area ratio is expected to decrease. Similarly at low current density as the flowrate is lower we expect high wetted area ratio. High wetted area ratio is associated with high liquid volume fraction in the cathode gas channels and therefore local surface coverage by liquid water is expected to be greater. Absence of adequate experimental data in this case restricts further validation of our model. The computed wetted area ratio in the cathode side is compared with the experimental data over a range of these operating conditions in Figs. 2–4. Fig. 2 depicts the model-experimental comparison for relative humidities of 67%, 45% and 25% at $I_{avg} = 0.2\,A\,cm^{-2}$ with cell temperature of 80 °C. Overall, good agreement is found (RMS (Root Mean Square) error is less than 0.06). At a medium current density of $0.5\,A\,cm^{-2}$, the match shown in Fig. 3 is also reasonable (RMS error is less than 0.08) except that the present model overpredicts at relative humidity of 67% for large air stoichiometry. The match between experimental results and numerical predictions shown in Fig. 4 is again good (RMS error is less than 0.04) at a high current density of $0.8\,A\,cm^{-2}$. These comparisons shown in Figs. 2–4 demonstrate that our model can predict the wetted area ratio reasonably well for a range of practical operating conditions.

The wetted area ratio less than unity, as displayed in Figs. 2–4, physically implies that the flow channels are partially dry (free of any liquid water) and partially wet due to liquid water accumulation, and that there exists a dry-to-wet transition within the channel length [32,36]. The results shown in Figs. 2–4 clearly indicate that the flow channels have a longer wet portion under high inlet humidity, lower air stoichiometry and lower current density, as expected.

The pressure drop along the cathode channels of the PEFC is compared between experimental measurements [27] and the present calculations, as shown in Fig. 5. Note that GDL intrusion to reduce cross-sectional areas of flow channels must be accounted for, as intrusion of soft GDL material into flow channels is inevitable during assembly of PEFCs. While it is difficult to quantify the degree of GDL intrusion *in situ*, we found 33% GDL intrusion at the edge channels yields a reasonable match with the experimental pressure drop data for all current densities, as shown in Fig. 5. The agreement is poor, particularly for the low current density of $0.2\,A\,cm^{-2}$. This may be due to the inadequacy of the present M^2 model to describe significant two-phase flow occurring at low current den-

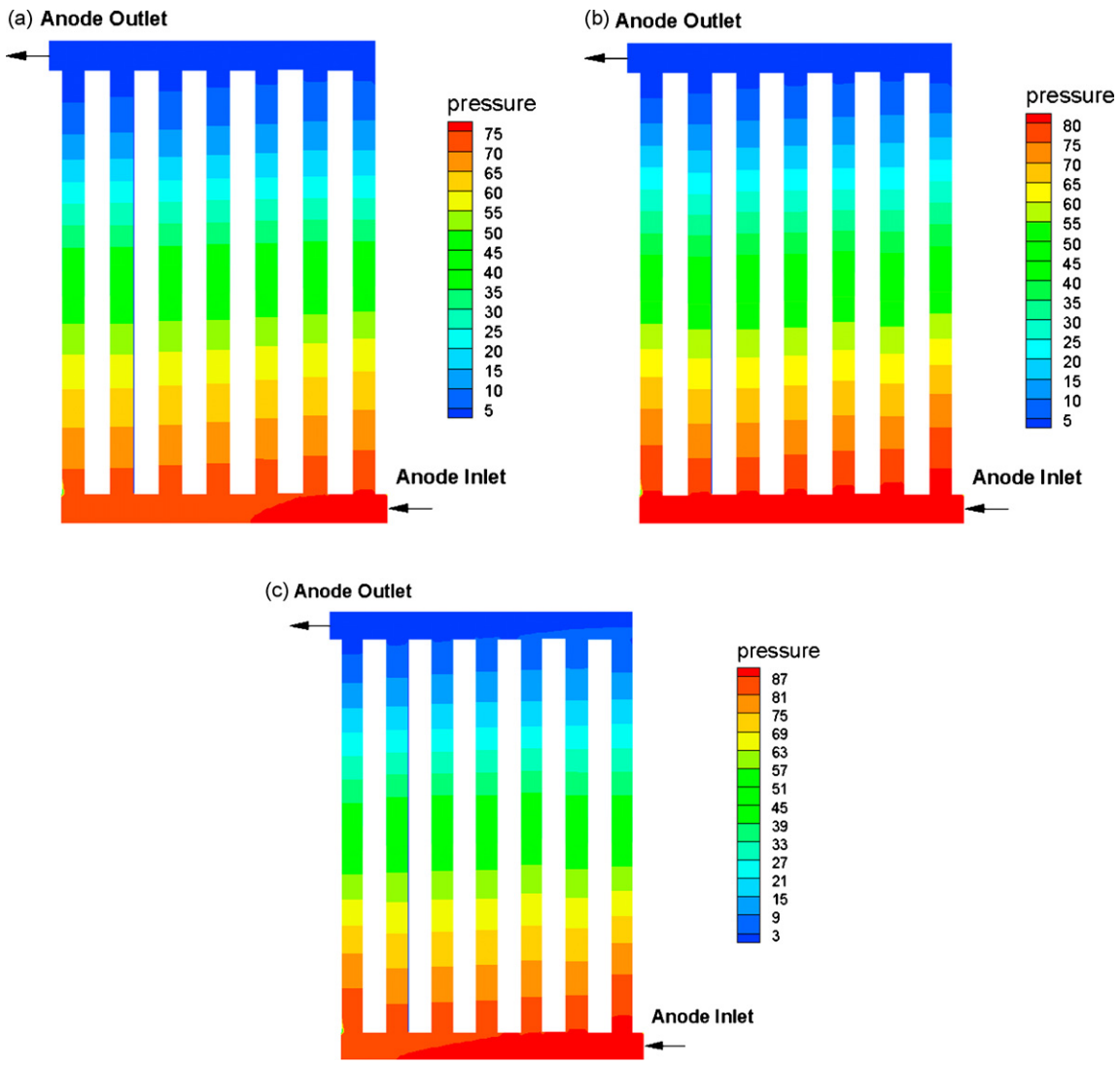

Fig. 10. Pressure (Pa) contour at the section of anode channels.

sities. Future investigation is needed to improve model accuracy in this regime.

5.2. Flow maldistribution and its effect on cell performance

While experimental validation has been carried out for system parameters, in this subsection we reveal the two-phase flow maldistribution in an operating PEFC and the impact on cell performance using the present model. All cases presented below use the cell temperature of 80 °C and relative humidity of 67%, most typical of automotive applications. The effect of GDL intrusion (Toray Paper TGPH-060) is studied for high current density (0.8 A cm^{-2}) and low stoichiometry (2.0). GDL intrusion of 17% and 33% at the two edge channels are considered to investigate the variation of flow maldistribution and the pressure penalty. The area maldistribution due to GDL intrusion changes the distribution of liquid water among channels and furthermore, interacts with the non-linear characteristics of two-phase flow to result in significant non-uniform distribution of reactants. The results of perfectly symmetric and intruded flow channels are compared and analyzed.

The current density distributions at the center of the membrane for perfect channels, 17% intruded channels and 33% intruded channels are displayed in Fig. 6. The contour shows somewhat symmetric current distribution over all seven channels for the perfect channel case. The slight non-uniformity among channels is caused by the fact that both inlet and outlet manifolds are included in the present computations. Flow resistance in the outlet manifolds of anode and cathode differs from that of the inlet manifold due to the presence of two-phase flow and changes with operating conditions. For the 17% intruded channels, there is an additional reduction in the flow cross-section of the two edge channels and the local current density there is lower. This uneven distribution in current density from channel to channel is more severe for the 33% intrusion. Clearly, this is caused by low reactant flows through the intruded channels. Furthermore, it is seen from Fig. 6 that local current density is usually smaller over the area of a land separating two flow channels. Note that the two edge channels are bounded by a half land on the edge of the cell. The low current density regions resulting from flow maldistribution decreases the cell performance as well as the utilization of precious-metal catalysts.

The pressure contours along the cathode channels are shown in Fig. 7 for the same cases. The pressure penalty increases by about 10% for the 33% GDL intrusion. Interestingly, the predicted pressure drop for 33% intrusion is closest to the experimental measurement. The experimental pressure drop for this case is 460 Pa and numerically predicted pressure drop is 423 Pa. At the same time the pressure drop for perfect channels is much less than the experimental data. This suggests the presence of GDL intrusion in flow

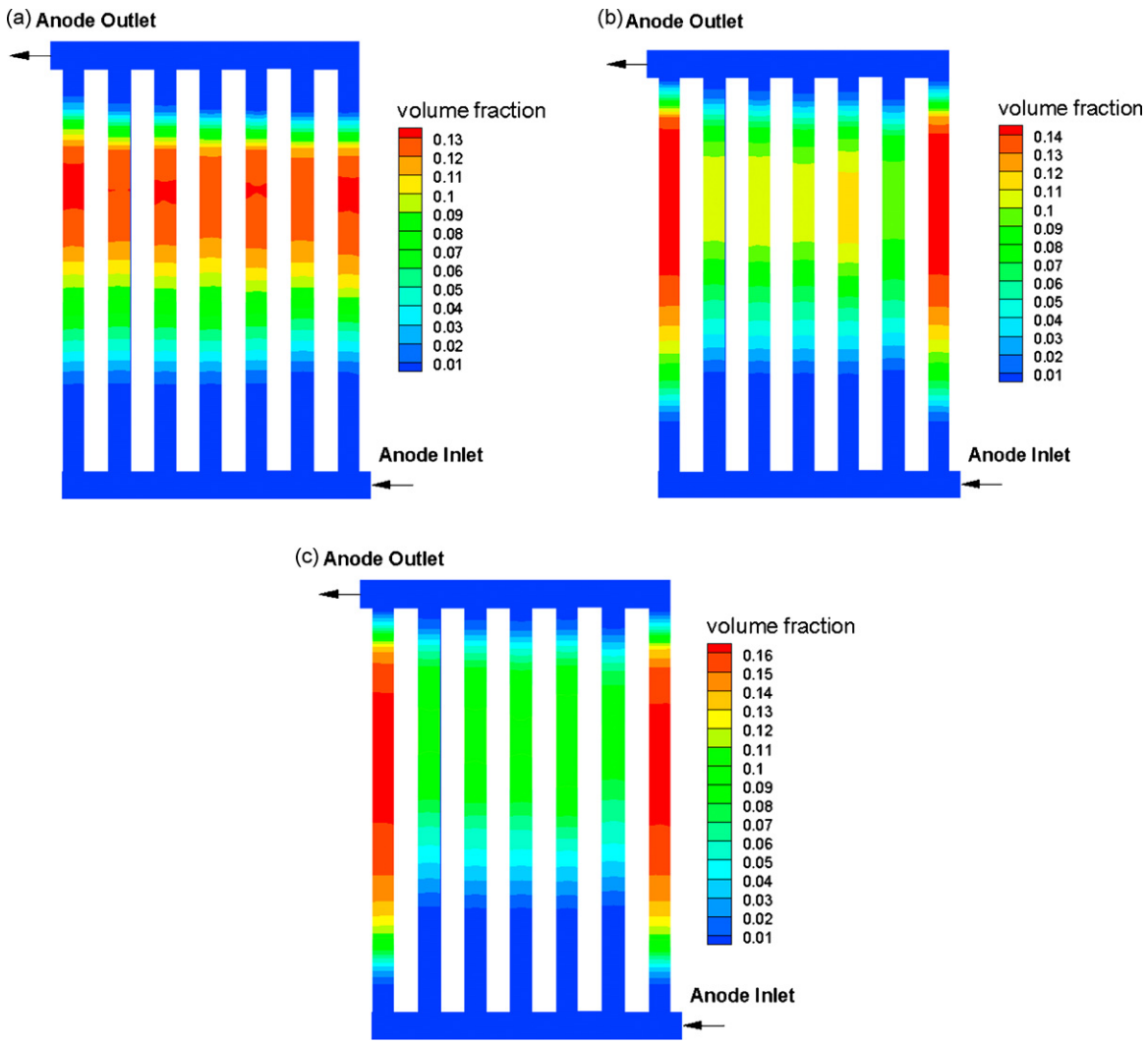

Fig. 11. Liquid water volume fraction at the section of anode channels.

channels and the extent of area maldistribution likely to be close to 33%. The liquid volume fraction contours in the cathode channels for the same cases are displayed in Fig. 8. The dry-to-wet transition is clearly visible in all cases. With GDL intrusion, the maximum liquid volume fraction occurs in the intruded channels and the liquid front is pushed considerably upstream. This is because the intruded channels feature larger flow resistance and hence lower gas velocity, thereby accumulating more liquid water. The presence of more liquid water further increases the flow resistance and reduces the gas flow through the channel. This feedback mechanism results in a 'U' shape of flow distribution across seven channels.

The liquid water saturation in the midsection of the cathode GDL for these three cases is plotted in Fig. 9. It is seen that the liquid saturation is much higher in the GDL, reaching about 30%. Maximum liquid water saturation appears over the lands at about the mid-length of the channels. For the unintruded channels (Fig. 9a) the liquid water saturation profiles exhibit a similar pattern. Interestingly, Fig. 9b and c show that the liquid water saturation in the GDL decreases in the vicinity of the intruded channels, possibly due to lower current density (see Fig. 6b and c). The effect of GDL intrusion on cell operation can be summarized by comparing Figs. 7–9. The current production is low over the intruded channels due to low reactant flowrate. As a result, water production is low and therefore the liquid saturation in the GDL is low over the intruded edge channels. Intuition suggests that the liquid water would be less in the intruded channels since less water is produced, but the ability of these channels to remove liquid water out of the cell is so low that more liquid water accumulates in the intruded channels.

The pressure contours along the anode channels are shown in Fig. 10 for the same three cases. Pressure penalty also increases in the anode side due to the presence of two-phase flow. However, the magnitude of the anode pressure drop is about 20% of the cathode due to much lower hydrogen flowrate than air. The liquid water volume fraction contours along the anode channels are displayed in Fig. 11. Not only is the dry-to-wet transition captured in the anode channels but there is also a wet-to-dry transition. The latter transition occurs because the anode outlet is facing the cathode inlet where relatively dry air is fed into the cell which re-evaporates the liquid water in the anode channels. It is seen that GDL intrusion has a severe effect in the anode.

The liquid water saturation in the midsection of the anode GDL for these three cases is plotted in Fig. 12. It is seen that the liquid saturation is much higher in the GDL than the anode channels. The maximum liquid saturation occurs over the lands in the middle of the cell, ranging from 23% to 25%. Once again, for the unintruded channels (Fig. 12a) the liquid saturation profiles are relatively symmetric from channel to channel, while there is clearly more liquid water in the GDL over the land area towards the center of the cell with intruded edge channels. This behavior of liquid water maldistribution resembles the cathode side.

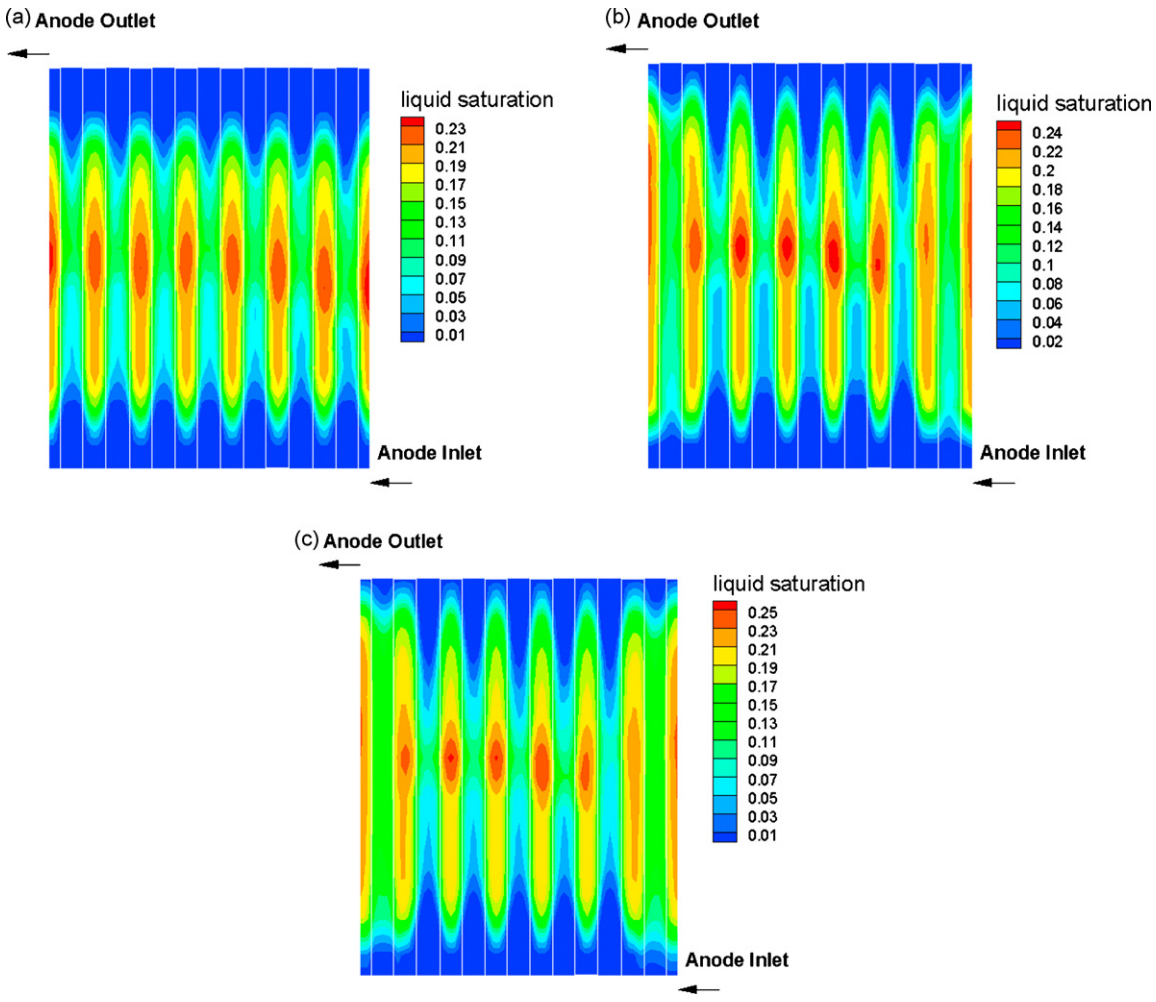

Fig. 12. Liquid water saturation contours at the midsection of the anode GDL.

Flow and liquid water maldistribution can be better depicted by liquid water volume fraction contours in the center of the channels along the in-plane direction. Fig. 13 compares these contour plots for a middle channel and an edge channel for the three cases of interest. For the perfect channels the axial profile of liquid water is very similar between the two channels (Fig. 13a). Along the cathode channel, a dry-to-wet transition can be seen, while the cathode exit always remains wet. In the anode channels, however, there exists dry–wet–dry transition, the physics of which has been elaborately discussed in the literature [32,35], albeit in the absence of two-phase flow in channels. Our results illustrate a profound effect of two-phase flow in channels on the liquid water distribution in the PEFC. That is, the wet-to-dry transition in the cathode is predicted without channel two-phase flow but not with the consideration of channel two-phase flow. This is because the channel two-phase flow allows for the accumulation of a large amount of liquid water, which then becomes difficult to dry up by dry gas from the anode inlet. For the same reason, however, the anode flow stream is prone to dryout because the anode flowrate is only about one-fifth of that of the cathode side.

The effect of area maldistribution on liquid water distribution is more evident from Fig. 13b. It is shown that the amount of liquid water is much higher in the edge channel section for 17% GDL intrusion. The dry-to-wet transition in the cathode occurs further upstream in the edge channel with respect to the middle channel. For the case with 33% GDL intrusion these effects are further magnified as shown in Fig. 13c. The difference in the maximum liquid water volume fraction between the channels is quite substantial. The wetted area is much higher for edge channels as well. Schematic diagrams illustrating the dramatic effect of GDL intrusion on liquid water distribution are given in Fig. 14a and b for the middle (unintruded) and edge (intruded) channels, respectively.

The local stoichiometry in each of the seven channels, defined as $\xi_{avg}(Q/Q_{avg})$ with Q being the local gas flowrate through a certain channel, is shown in Fig. 15 to quantify the degree of flow maldistribution. Such plots for both cathode and anode sides are shown in Fig. 15. The channels are numbered starting from the inlet in each case. It can be seen that the flow maldistribution is relatively minor in perfect channels and arises solely from two-phase flow. When GDL intrusion is considered, severe maldistribution of flow develops in the edge channels. Area reduction of 17% at the edge channels results in about 25% reduction in flowrate. Similarly, for 33% area reduction at the edge channels, the reactant flow decreases by almost 50%, while the flows through the other channels without GDL intrusion do not vary much. These observations are true for both the cathode and anode channels. In the present cases, the average flow stoichiometry over the entire cell is 2.0 in both anode and cathode. A reduction of 50% flow means that the local stoichiometry is less than 1.0, insufficient to sustain the average reaction rate and potentially leading to detrimental side reactions such as oxygen evolution and carbon corrosion.

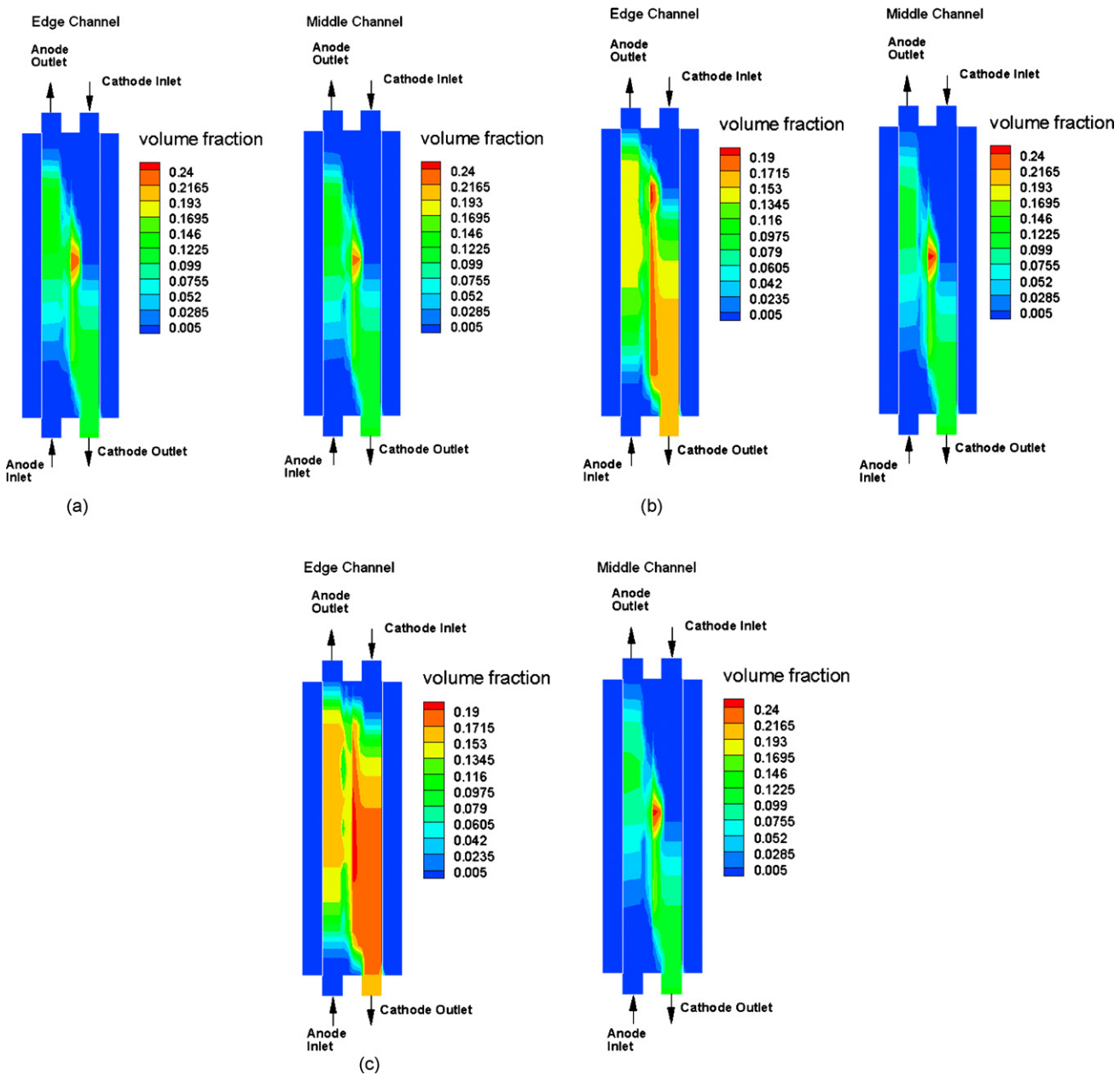

Fig. 13. Liquid water saturation contours across edge and middle channels.

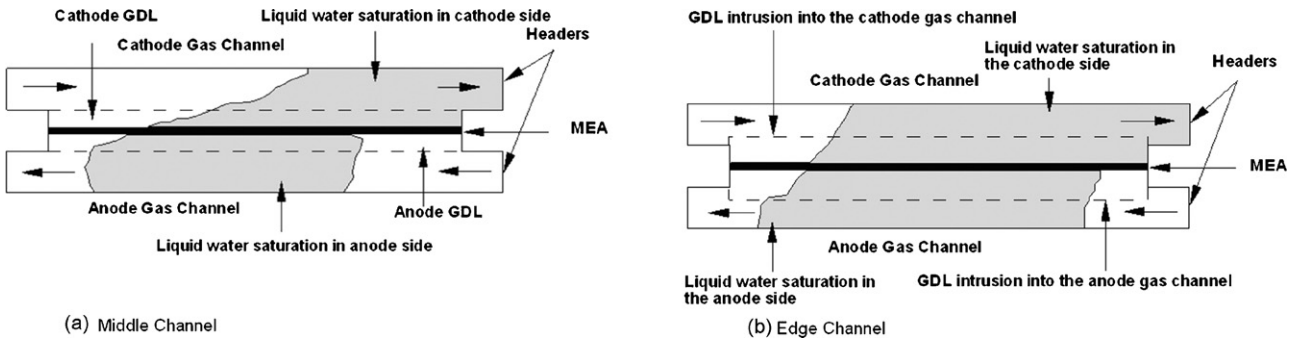

Fig. 14. Schematic of liquid water distribution in a PEFC.

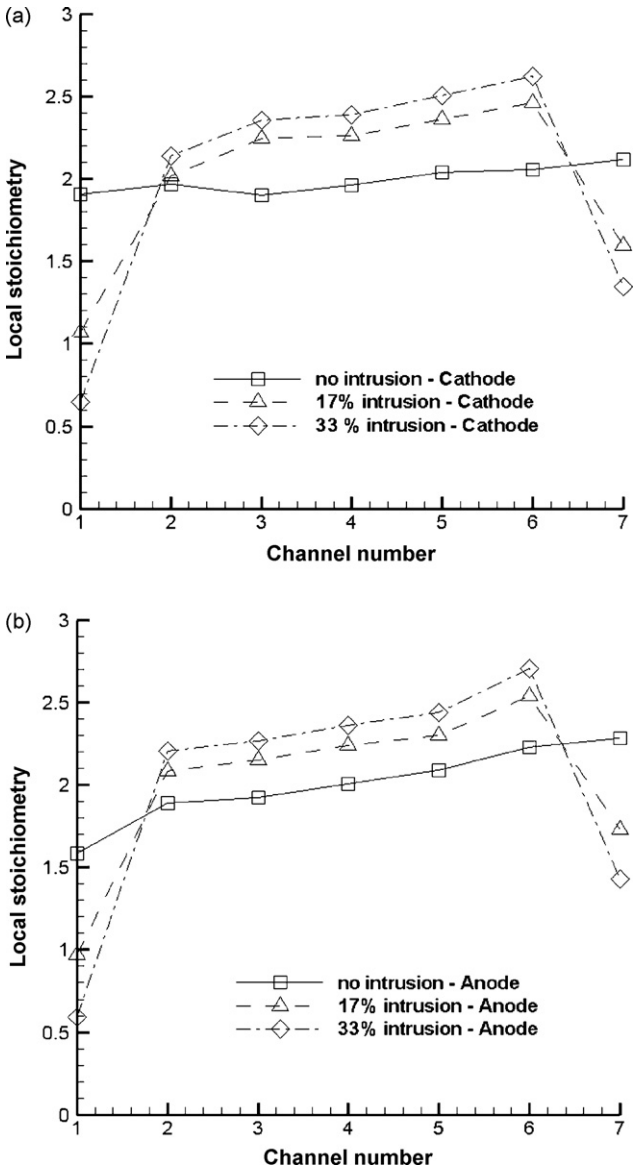

Fig. 15. Plots of local flow stoichiometry in different channels on the cathode and anode sites.

6. Conclusion

A channel two-phase flow model has been integrated with the previously developed two-phase PEFC model based on the M^2 framework. The complete PEFC model considering two-phase flow in channels is employed to explore flow maldistribution in an operating PEFC for the first time. The wetted area ratio on the cathode GDL surface predicted by the present model matches quantitatively with experimental data over a range of current density, relative humidity and flow stoichiometry. In addition, the overall pressure drop prediction is found to be good.

The effect of GDL intrusion at the edge channels, as commonly observed in a fuel cell stack, is numerically studied. Severe flow and liquid water maldistributions are predicted due to GDL intrusion in the edge channels. Low flowrate of the intruded channels make these regions starved of reactants, thus reducing the cell performance and durability. Innovative flow field designs are needed to mitigate flow maldistribution and ensuing adverse impact on cell performance and durability.

Acknowledgements

We acknowledge NSF grant no. 0609727 and industrial sponsors of ECEC for financial support of this work.

References

[1] J. Larminie, A. Dicks, Fuel Cell Systems Explained, second edition, John Wiley, 2003.
[2] C.Y. Wang, Chem. Rev. 104 (2004) 4727–4766.
[3] S. Um, C.Y. Wang, K.S. Chen, J. Electrochem. Soc. 147 (2000) 4485–4493.
[4] S. Dutta, S. Shimpalee, J.W. Van Zee, Int. J. Heat Mass Transf. 44 (2001) 2029–2042.
[5] U. Pasaogullari, C.Y. Wang, J. Electrochem. Soc. 151 (2004) A399–A406.
[6] X.G. Yang, F.Y. Zhang, A. Lubawy, C.Y. Wang, Electrochem. Solid-State Lett. 7 (2004) A408–A411.
[7] F.Y. Zhang, X.G. Wang, C.Y. Wang, J. Electrochem. Soc. 153 (2006) A225–A232.
[8] Z.H. Wang, C.Y. Wang, K.S. Chen, J. Power Sources 94 (2001) 40–50.
[9] D. Natarajan, T.V. Nguyen, J. Electrochem. Soc. 148 (2001) A1324–A1335.
[10] S. Mazumder, J.V. Cole, J. Electrochem. Soc. 150 (2003) A1510–A1517.
[11] U. Pasaogullari, C.Y. Wang, J. Electrochem. Soc. 152 (2005) A380–A390.
[12] Y. Wang, C.Y. Wang, J. Electrochem. Soc. 153 (2006) A1193–A1200.
[13] K. Promislow, J. Stockie, B. Wetton, Proc. R. Soc. A 462 (2006) 789.
[14] E.S. Lee, Proceedings of FEDSM 2005, ASME Fluids Engineering Division Summer Meeting and Exhibition, Houston, TX, USA, June 19–23, 2005.
[15] F. Barrears, A. Lozano, L. Valiano, C. Marin, A. Pascau, J. Power Sources 144 (2005) 54–66.
[16] Y.G. Yoon, W.Y. Lee, G.G. Park, T.H. Yang, C.S. Kim, Electrochim. Acta 50 (2/3) (2004) 709–712.
[17] S. Shimpalee, S. Greenway, J.W. Van Zee, J. Power Sources 160 (1) (2006) 398–406.
[18] X.D. Wang, Y.Y. Duan, W.M. Yan, J. Power Sources 172 (1) (2007) 265–277.
[19] X. Liu, H. Guo, F. Ye, C.F. Ma, Electrochim. Acta 52 (11) (2007) 3607–3614.
[20] D. Spernjak, A.K. Prasad, S.G. Advani, J. Power Sources 170 (2) (2007) 334–344.
[21] X. Li, I. Sabir, J. Park, J. Power Sources 163 (2) (2007) 933–942.
[22] G. He, P. Ming, Z. Zhao, A. Abudula, Y. Xiao, J. Power Sources 163 (2) (2007) 864–873.
[23] P. Quan, M.C. Lai, J. Power Sources 164 (1) (2007) 222–237.
[24] X. Zhu, P.C. Sui, N. Djilali, J. Power Sources 172 (1) (2007) 287–295.
[25] K. Jiao, B. Zhou, P. Quan, J. Power Sources 154 (1) (2006) 124–137.
[26] K. Jiao, B. Zhou, P. Quan, J. Power Sources 157 (1) (2006) 226–243.
[27] I.S. Hussaini, C.Y. Wang, J. Power Sources 187 (2) (2009) 444–451.
[28] Y. Wang, S. Basu, C.Y. Wang, J. Power Sources 179 (2008) 603–617.
[29] S. Basu, C.Y. Wang, K.S. Chen, ASME J. Fuel Cell Sci. Technol. 6 (3) (2009), in press.
[30] H. Meng, C.Y. Wang, J. Electrochem. Soc. 151 (2004) A358–A367.
[31] Y. Wang, C.Y. Wang, J. Electrochem. Soc. 154 (2007) B636–B643.
[32] H. Ju, G. Luo, C.Y. Wang, J. Electrochem. Soc. 154 (2007) B218–B228.
[33] C.Y. Wang, P. Cheng, Int. J. Heat Mass Transf. 39 (1996) 3607–3618.
[34] T. Berning, N. Djlali, J. Electrochem. Soc. 150 (2003) A1589–A1598.
[35] H. Meng, C.Y. Wang, Chem. Eng. Sci. 59 (2004) A3331–A3343.
[36] G. Luo, H. Ju, C.Y. Wang, J. Electrochem. Soc. 154 (2007) B316–B321.